Role of friction and geometry in tuning the bending stiffness of topologically interlocking materials

Tracy Lu[a,1], Ziran Zhou[a,1], Punnathat Bordeenithikasem[b], Norman Chung[a], Diana Frias Franco[a], Jose E. Andrade[a], Chiara Daraio[a,2]

[a]*Department of Mechanical and Civil Engineering, California Institute of Technology, 1200 E. California Blvd, Pasadena, 91106, California, USA*
[b]*NASA Jet Propulsion Laboratory, California Institute of Technology, 4800 Oak Grove Dr, Pasadena, 91109, California, USA*

Abstract

Topologically interlocking material (TIM) systems offer adjustable bending stiffness controlled by external pre-stress, as shown in previous studies. This study focuses on a specific TIM system comprised of truncated tetrahedral particles interconnected via tensioned wires. The fabrication process involves weaving nylon wires through 3D printed truncated tetrahedrons that have longitudinal and latitudinal through-holes. By varying the tension applied to the wires, one can systematically control the overall bending stiffness of the TIM system. We change the surface friction and the contact angle between adjacent particles at a fixed wire tension, to study experimentally how they affect the system's bending response. We inform experiments with Level Set Discrete Element Method (LS-DEM) simulations, to correlate surface friction and contact area changes with the system's bending modulus. The numerical model is shown to be predictive and could be used in the future to evaluate designs of TIMs.

Keywords: tunable bending stiffness, topologically interlocking materials, woven architected materials, level set discrete element method

---

[1] These authors contributed equally.
[2] Corresponding Author. Email: daraio@caltech.edu

1. Introduction

The demand for materials with adjustable physical properties and the ability to respond rapidly to environmental stimuli has been growing [1]. In particular, fabrics with adaptable or tunable stiffness are applicable for use in soft robotics, shape morphing structures, and wearable devices [2, 3, 4]. For example, tunable fabrics can find use in wearable medical devices, like exoskeletons, haptic systems, and reconfigurable medical supports [5, 6, 7]. At larger scales, applications of tunable fabrics include transportable and reconfigurable architectures, which transition from a compact and flexible state to a deployed and rigid state [8, 9].

Incorporating interlocking particles in fabrics opens up the possibility to incorporate added structural support and adjustable mechanical properties [10, 11, 12, 13]. The mechanical behavior of such structured fabrics or topologically interlocking materials (TIM) is determined by the characteristics of their constituents and the topology of their arrangement [14, 11, 15, 16]. In most architected materials and woven fabrics, these mechanical behaviors are determined during the design process and remain fixed after the components are fabricated. However, in some realizations, the fabric properties can be adjusted through actuation [13, 17]. Wang, et al. demonstrated architected fabrics consisting of chain mail layers with interconnected particles, which demonstrate the ability to reversibly and gradually switch between soft and rigid states [2, 16, 17]. The control of the fabrics' stiffness is achieved by applying pressure at the boundary that jams the particles via vacuum suction, in a system similar to other structured fabrics [2, 4, 8]. While this example demonstrates the ability to create architected fabrics with tunable properties, the use of vacuum actuation is not practical, because it requires bulky and energy intensive pumping systems. Using tensioned fibers or artificial muscles could be a more compact and power-efficient solution [18].

In this paper, we study the response of a particular TIM system, consisting of truncated tetrahedral particles connected by woven tension wires [13, 15, 16]. This fabric-TIM system exhibits a tunable bending modulus in response to varying levels of applied tension in the wires [17, 16]. Unlike TIM systems solely held in place by external confinement [13], the fabric-TIM systems with adjustable or actuatable tension allow for stiffening and softening, as shown in Fig. 1c and d. However, the adjustable feature of the fabric-TIM is not the focus of this manuscript. To better understand the fundamental mechanisms governing the tunability of the TIM system's apparent bending stiffness, we explore the role of contact angle and contact friction, using experimental results and numerical simulations.

2. Design and Fabrication of the Topologically Interlocking Materials

There are distinct approaches in the design of TIMs. For example, Molotnikov, et al. [17] demonstrated a TIM system made of osteomorphic blocks that are woven together to form an interlocked state. Dyskin, et al. [10] have chosen the main constituent building block geometries as truncated tetrahedron particles, some with longitudinal and latitudinal through-holes for weaving with shape memory alloy wires [16]. Tetrahedrons are the simplest platonic solid, and all platonic solids can be arranged into layer-like structures in which they are interlocked topologically [19]. Additionally, trapezoidal particles are known for their substantial contact surfaces [12] and have extensive applications in architected materials to enhance mechanical performance [20].

For this work, we study a classic, model system of a TIM assembled with truncated tetrahedron particles as the basic building blocks (Fig. 1a). Using truncated tetrahedrons, as opposed to osteomorphic blocks, allows us to systematically change a single parameter, such as dihedral angle, to dictate the amount of interlocking. Moreover, since truncated tetrahedrons don't completely fit into each other, the relaxed state is more flexible and similar to a fabric. The particles are designed to be printed with longitudinal and latitudinal through-holes. We use nylon wires to weave through each discrete particle and interconnect them, as depicted in Fig. 1b. To actuate the fabrics, we apply different levels of tension to the wires and thereby jam the particles with their neighbors to form an interlocked state (Fig. 1c–d). The combined outer surface of the truncated tetrahedrons upon post-tensioning is a flat plane. The resulting assemblies possess geometric contact and interlocking periodicity.

A series of TIMs were produced by varying two different particle parameters: the particle's dihedral angles, θ (Fig. 1a) and their surface friction. The particles were fabricated with three different dihedral angles, 60°, 70° and 90°, where the latter is simply a prism geometry with no geometric interlocking. To vary the surface friction, we 3D-printed the particles using two different materials of similar stiffness: Vero White (VW) using an Objet Stratasys Connex 500, and Nylon Polyamide 12 (PA12) using a Sintratec

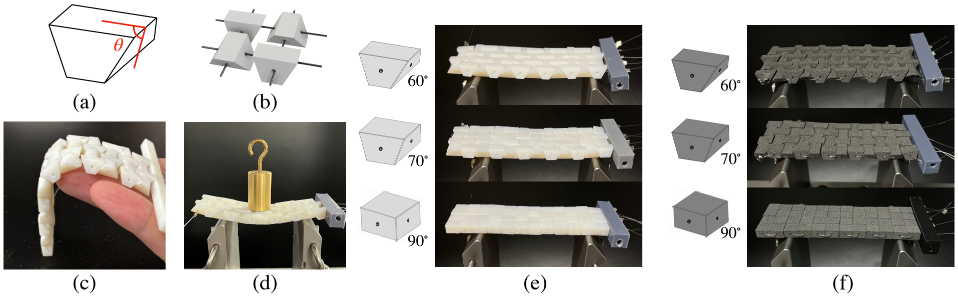

Figure 1: (a) Schematic of a basic building block (particle) in the shape of a truncated tetrahedron [10], with dihedral angle, θ, between the truncating surface and the side surface of particle; (b) Schematic of particles inter-connected by post-tensioned wires; (c) Unactuated, soft state of the sample; (d) Actuated, stiff state of the sample; (e-f) Samples made by particles with $\theta = 60^\circ$, 70° and 90°; Samples shown in (e) are made by Vero White, with a measured friction coefficient of 0.2; samples shown in (f) are made by Nylon Polyamide 12, with a measured friction coefficient of 0.6.

SLS 3D printer. Particles were cleaned by removing the outer support material. The Vero White particles were additionally cleaned in a 2 percent aqueous solution of NaOH to remove the remaining support material. The coefficients of friction were determined experimentally after the particles had been cleaned, using custom-designed sliding apparatuses. The resulting surface friction coefficients were measured to be 0.2 and 0.6, respectively. The particles were then woven together with 0.3 mm diameter nylon wire. The system is subsequently actuated with a small motor (28BYJ-48 Stepper Motor) that controls the amount of wire tension and therefore jamming the particles. A custom-designed fixture was 3D-printed for the motor housing and tensioning mechanism with sufficient clearance space for the tension meter (Checkline ETB-2000). The tension should attain the predetermined threshold, ensuring that the wire remains within the elastic range during the testing phase. The tension meter was used to gauge the tension and determine whether to incrementally increase the tension by spinning the motor. Once the desired average tension was achieved in the wires, the tension was secured with clamp beads to hold the wire in place. Then the woven sample was removed from the fixture with the motor.

3. Simulations

For a more systematic analysis of the TIM fabrics' behavior as a function of particle's geometry and constituent material properties, a reliable and validated numerical model is necessary. Level Set Discrete Element Method (LS-DEM) is used to model the physical experiment. LS-DEM is a variant of the traditional Discrete Element Method (DEM) allowing arbitrary object shapes. Originally developed for granular applications [21, 22], LS-DEM has recently been adapted to study the seismic behaviors of multi-block structures [23, 24], and the structural analysis of TIM, showing satisfactory results in capturing the slip-governed failure [25, 26] and the deflection limit [27] of the slab-like TIM. LS-DEM uses level set functions as the geometric basis, which calculates the signed distance ϕ from any arbitrary point in the space to the nearest surface of the grain. For example, in this work, a cross-sectional slice of a basic building block, which is the shape of a truncated tetrahedron, is a trapezoid in 2D, as shown in Fig. 2a. The surface of the building block, or particle, can be reconstructed by $\phi = 0$. We impose a set of surface nodes with uniform discretization size onto each particle (Fig. 2b). When checking potential particle contact, we take the position of each surface node $\mathbf{x}$ of one particle and check the corresponding level set value from another neighboring particle. If $\phi(\mathbf{x}) \leq 0$, then contact exists between this pair of particles.

Given the discrete nature of the woven-connected particles, LS-DEM is capable of extracting particle-scale information at micro-mechanical level, thus providing insight into how friction and contacts between particles affect the macroscopic property such as sample bending stiffness. Furthermore, the use of level set function provides flexibility in particle shape control, allowing us to easily simulate different particle shapes and investigate the combined geometric shape effects to the sample's overall behavior. The use of LS-DEM is also computationally efficient compared to other simulation methods such as finite element method (FEM) for potential simulations of large ensembles of particles [28].

We use point forces acting on the boundary particles T_{BC} to model the post-tensioning effect of the wires (Fig. 2d). On top of that, we use massless springs connecting the face center of the side of each particle to the face center of the side of its neighbors (Fig. 2c). The neutral position of the spring is at a distance $\bar{d} = 0$. The springs connecting neighboring particles can only exert tensile forces on the connected particles. When two neighboring particles are

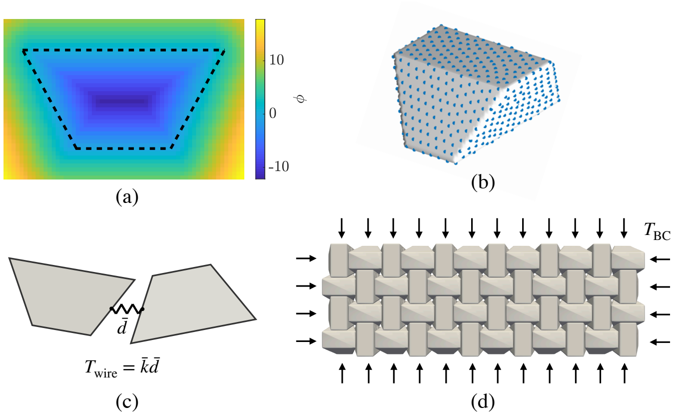

Figure 2: (a) Illustration of the level set matrix of a slice of the truncated tetrahedron; (b) The particle is reconstructed by surfaces with $\phi = 0$; the imposed surface nodes are shown in blue dots; (c) Illustration of a pair of neighboring particles, connected by a massless spring with stiffness $\bar{k}$ and elongation $\bar{d}$; (d) Illustration of the sample under post-tensioning force T_{BC}.

separated, the wire force T_{wire} is calculated as

$$T_{\text{wire}} = \bar{k}\bar{d} \tag{1}$$

where $\bar{k}$ is the stiffness of the spring and is calibrated to match the experimental result of an uniaxial tension test carried out on a single woven wire.

4. Mechanical Characterizations

In order to experimentally investigate the macroscopic properties of the sample under various particle geometries and material properties, displacement-controlled three-point bending tests were performed with an Instron E3000 Mechanical Testing Machine (Fig. 3a). The indenter had a set loading rate of 0.5 mm s^{-1}. To ensure that the TIM systems deform within their components' elastic limits, we imposed a maximum indentation depth of 5 mm. This indentation depth was determined by testing on 3D-printed homogeneous solid counterparts of the same material with the same fabric sample dimensions. The three-point bending tests show no yielding behavior within 5 mm. This indentation depth also guarantees that the wire remains within its elastic limit, confirmed by independent experiments testing the elastic limit of the wire, aligning with the assumption made in Eqn. 1.

To compare the bending performance of the different fabrics, we define an apparent elastic bending modulus, E^*, as [2]:

$$E^* = \frac{KL^3}{4bh^3}. \tag{2}$$

Here, K is the stiffness of the initial linear regime of the force-displacement plot obtained from the test machine, L is the support span, b is the width of the sample, and h is the thickness of the sample before testing.

We study the role of friction and particle's shape on the overall fabric's behavior, comparing the apparent bending moduli values extracted from the experiments. Fig. 3b shows an overview of the bending modulus calculated from Fig. 3c–d. using Eqn. 2. Both increasing surface irregularities (i.e., friction between particles) and geometric interlocking have a positive correlation with the bending modulus. Samples made with PA12, resulting in a higher surface friction coefficient ($\mu = 0.6$) than those made with Vero White (VW) ($\mu = 0.2$), exhibit almost twice as much bending modulus as VW samples of the same particle geometry. Fig. 3c–d show the force-displacement plot for VW samples and PA12 samples accordingly. The force-displacement curves obtained from the three-point bending tests show an initially linear regime at small indentation depths, primarily due to the elastic response of the wire while the particles spread out. However, as the displacement increases, a nonlinear response is observed, most likely because of frictional sliding and local rearrangement of the particles within the system. Comparing the force-displacement plot within samples of the same material (Fig. 3c–d), we see that particles with smaller dihedral angle θ, which result in higher interlocking upon post-tensioning, show higher stiffness. If we compare samples of same particle geometry but made with different materials, samples with higher surface friction show higher stiffness.

To construct the numerical model, we first construct the particles using level set functions and surface nodes (Figure 2a–b). We then arrange and post-tension the particles (Figure 2c–d), as described in Simulations section. To simulate the testing setup, we construct a 1:1 model of the experiment apparatus using the same level set technique (see Appendix). We then move the indenter downward at a constant loading rate. In the experiments, though the fabrics samples are prepared and post-tensioned according to the same standard, there is no way to explicitly measure the slack of wires introduced during fabrication, and consequently it is not possible to know the exact tensile forces, T_{BC}, exerted by the wires on all particles. Therefore, we adjust

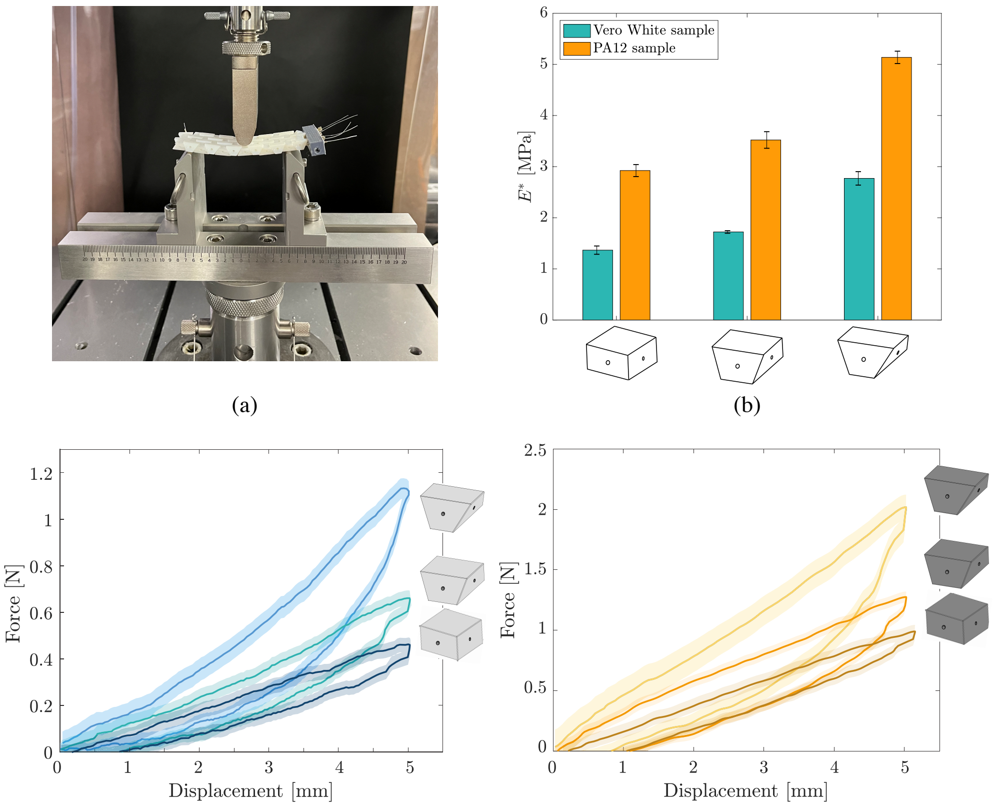

(a) (b)

(c) (d)

Figure 3: (a) The three-point bending test setup with sample; (b) Apparent bending modulus of the different samples, fabricated with 2 different constitutive materials (Vero White and PA12) and three different dihedral angles ($\theta = 60°$, $70°$ and $90°$); (c) Force-displacement plots of the Vero White samples; (d) Force-displacement plot of the PA12 samples. In (c) and (d), for each sample, a total of five experiments are performed. The solid lines represent the average force-displacement behavior, and the shaded regions show the standard deviation over five experiments.

the boundary force T_{BC} in the bending simulation of the 70° VW sample until the simulated apparent bending modulus E^* matches with that of the corresponding experiment. To ensure consistency and uniformity, we then apply the same calibrated boundary force to the remaining five simulations (60° and 90° VW samples, as well as 60°, 70° and 90° PA12 samples).

As depicted in Fig. 4, the resulting calibrated numerical model exhibits good agreement with experimental data regarding the apparent bending

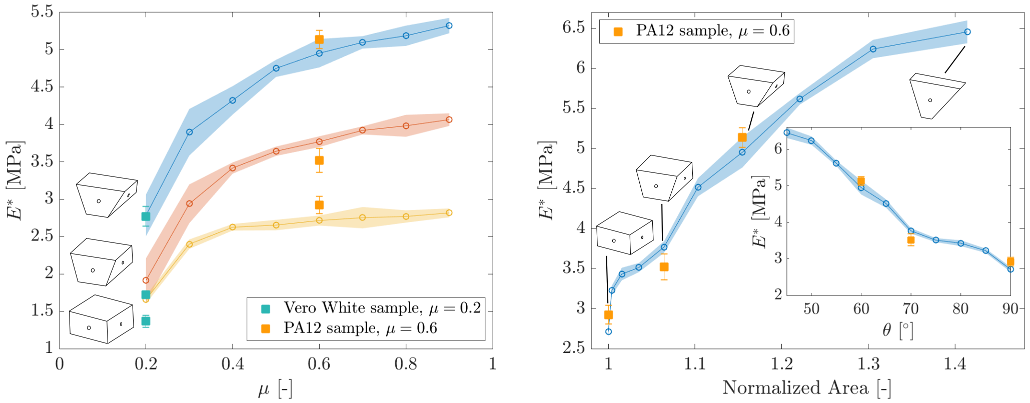

(a) (b)

Figure 4: Comparison of experiments and numerical simulations. (a) Simulated bending modulus of samples consisted of particles with $\theta = 60°$, $70°$ and $90°$ across different friction coefficient, from 0.2 to 0.9. For each particle shape at each friction coefficient, five simulations are run. For each run, noise is introduced to the initial particle position, particle orientation and boundary force T_{BC}. The solid line represents the average modulus, while the shaded regions show the standard deviation across five runs. Experiment results obtained from VW ($\mu = 0.2$) and PA12 ($\mu = 0.6$) samples are marked by green and orange respectively; (b) Simulated bending modulus vs. normalized contact area with particles from $\theta = 45°$ to $\theta = 90°$ with 5° increments. The contact area is normalized by the contact area of the 90° particle. Inset: simulated bending modulus vs. θ. Similar to (a), five simulations are run for each particle shape and noise is introduced in the initial state of each simulation. Experiment results from PA12 are marked in orange.

modulus E^*. In Fig. 4a, we show that as the friction coefficient reaches larger values (>∼0.3), the bending modulus of the samples does not increase as much, particularly for the samples with the least geometric interlocking (rectangular prism particles). As expected, in samples with more interlocked particles, the modulus increases more rapidly with increasing friction coefficient. For the 90° prism particles, the interwoven wire and friction between neighboring particles are the main factors that counteract out-of-plane deflection. With the most interlocked particles (60° prism particles), however, not only friction and the wire, but also geometric constraints are collectively counteracting the out-of-plane deflection.

In order to analyze how geometry affects the modulus, we simulate the bending tests of samples made by 7 other particles of different degrees of geometric interlocking. Wang et al. [2] reported a quadratic law relating average particle contact number to the apparent bending modulus. In this work, since all particles are generated with surface nodes of uniform discretization size, the contact number per particle upon contact directly translates to contact area between the contacting neighboring particles. Since we are assuming a small indentation depth, we estimate the contact area to be the maximum area of a side surface of the truncated tetrahedron, which is trapezoidal. We plot the bending modulus against the maximum contact area accordingly. From Fig. 4b, we see that the bending modulus scales almost linearly with the contact area and the dihedral angle θ, showing that the particle geometry is a crucial factor in contributing to the bending modulus.

We attribute the quasi-linear scaling between the contact area and the bending stiffness in our samples to the presence of the woven wires, which make the samples of less geometric interlocking rely more on elastic wire forces. During indentation, the wires in samples made from the rectangular prism particles are expected to be stretched more compared to samples made from the 45°-particles. This indicates that the wires may exert increased anti-separation forces within the 90°-particle TIMs in contrast to the other particles that can rely on greater geometric interlocking.

5. Conclusion

In this paper, we study the role of particles' geometry and inter-particle friction in the bending response of TIM systems consisting of truncated tetrahedron particles woven together with nylon wires. We fabricate samples with particles of varying interlocking contact angles and surface friction. In post-tensioned state, we find that both high friction and large geometric contact area between the neighboring particles contribute positively to the resulting sample bending resistance. The positive effect of friction to bending stiffness diminishes as friction coefficient increases. The contact area positively contributes to the bending modulus at a linear rate.

The TIM is a complex system with many factors at play. Besides the friction and geometric interlocking, sample thickness and external post-stress also have profound effects on bending response. In order to isolate the effect of friction and geometry, we keep the sample thickness and post-stress consistent throughout all experiments and simulations. More comprehensive study on the combined effect of all factors should be investigated in future work.

Acknowledgement

Part of this research was done at the Jet Propulsion Laboratory (JPL), California Institute of Technology, under contract with NASA (80NM0018D0004). This work was supported by the JPL Researchers on Campus program and Caltech President's and JPL Director's Research and Development Fund. Reference herein to any specific commercial product, process, or service by trade name, trademark, manufacturer, or otherwise, does not constitute or imply its endorsement by the United States Government or the Jet Propulsion Laboratory, California Institute of Technology. J.E.A. and Z.Z. would like to acknowledge the support from the National Science Foundation (NSF) under award number CMMI-2033779, and the U.S. Army Research Office under grant number W911NF-19-1-0245.

Data availability

Data is available upon reasonable request.

Appendix A. Numerical model setup

Truncated tetrahedron particles are characterized by a level set grid of 2 mm/voxel. The surface nodes are discretized with a surface density of 230 points/cm^2. The contact mechanism of a pair of penetrating neighboring particles are estimated by visco-elastic models composed of linear springs and viscous dampers. The linear springs have normal and shear stiffnesses k_n and k_s. The choice of these parameters takes into account factors considering material modulus and TIM arrangements, ensuring no excessive overlap between contacting particles [25]. We assume the stiffnesses of the particles made of two materials are comparable. The viscous dampers have normal damping coefficient γ_n estimated based on coefficient of restitution C_res [29] by

$$\gamma_n = 2\sqrt{m k_\mathrm{n}} \frac{-\ln C_\mathrm{res}}{\sqrt{\pi^2 + \ln {C_\mathrm{res}}^2}}. \tag{A.1}$$

where m is the mass of the particles. LS-DEM uses an explicit time integration scheme. The critical time-step is estimated by [30]

$$\Delta t = 0.4\sqrt{\frac{2m}{5k_\mathrm{s}}}, \tag{A.2}$$

The wire stiffness $\bar{k}$ is calibrated to match the experimental result of a single woven wire in an uniaxial tension test. The set of parameters used in this work is documented in Table A.1.

Table A.1: Model parameters

Parameter	Value	Units
Normal particle stiffness k_n	2	MN/m
Shear particle stiffness k_s	2	MN/m
Wire stiffness $\bar{k}$	720	N/m
Friction coefficient μ	{0.2,0.3,. . . ,0.9}	-
Time-step Δt	5.6e-7	s
Coefficient of restitution C_res	0.5	-

We construct a 1:1 numerical model for the testing apparatus (Fig. A.5) with the same level set grid density and surface discretization density. The indenter and the two supports have the same dimension as the actual experimental test machine. The two supports are placed 6 cm apart, same as the experiment. After the numerical TIM sample has been post-tensioned, we allow the sample to settle onto the supports by gravity. We then move the indenter downward at a constant speed. Since we have a small time-step of $\Delta t = 5.6 \times 10^{-7}$ s for numerical stability, we apply a global damping parameter of $1 \times 10^{-4}/\Delta t$ s^{-1} to ensure quasi-static conditions and to avoid excessive computation time [21].

References

[1] M. Stoppa, A. Chiolerio, Wearable electronics and smart textiles: A critical review, Sensors 14 (7) (2014) 11957–11992. doi:10.3390/s140711957. URL `https://www.mdpi.com/1424-8220/14/7/11957`

[2] Y. Wang, L. Li, D. Hofmann, J. Andrade, C. Daraio, Structured fabrics with tunable mechanical properties, Nature 596 (2021) 238–243. doi:https://doi.org/10.1016/j.mechrescom.2018.07.002.

[3] S. Mondal, Phase change materials for smart textiles – an overview, Applied Thermal Engineering 28 (11) (2008) 1536–1550. doi:https://doi.org/10.1016/j.applthermaleng.2007.08.009.

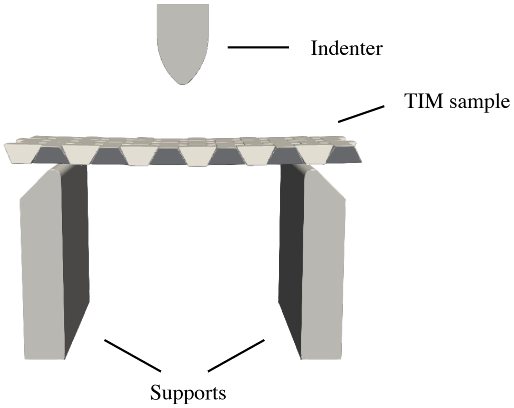

Figure A.5: Numerical test apparatus.

[4] D. S. Shah, E. J. Yang, M. C. Yuen, E. C. Huang, R. Kramer-Bottiglio, Jamming skins that control system rigidity from the surface, Advanced Functional Materials 31 (1) (2021) 2006915. doi:https://doi.org/10.1002/adfm.202006915.

[5] A. R. Ploszajski, R. Jackson, M. Ransley, M. Miodownik, 4d printing of magnetically functionalized chainmail for exoskeletal biomedical applications, MRS Advances 4 (23) (2019) 1361–1366. doi:10.1557/adv.2019.154.

[6] J. M. McCracken, B. R. Donovan, T. J. White, Materials as machines, Advanced Materials 32 (20) (2020) 1906564. doi:https://doi.org/10.1002/adma.201906564.

[7] X. Yang, Z. Wang, B. Zhang, T. Chen, C. Linghu, K. Wu, G. Wang, H. Wang, Y. Wang, Self-sensing robotic structures from architectured particle assemblies, Advanced Intelligent Systems 5 (1) (2023) 2200250. doi:https://doi.org/10.1002/aisy.202200250.

[8] J. Ou, L. Yao, D. Tauber, J. Steimle, R. Niiyama, H. Ishii, Jamsheets: Thin interfaces with tunable stiffness enabled by layer jamming, in: Proceedings of the 8th International Conference on Tangible, Embedded and Embodied Interaction, TEI ’14, Association for Computing Machinery, New York, NY, USA, 2014, p. 65–72. doi:10.1145/2540930.2540971.
URL `https://doi.org/10.1145/2540930.2540971`

[9] P. Aejmelaeus-Lindström, J. Willmann, S. Tibbits, F. Gramazio, M. Kohler, Jammed architectural structures: Towards large-scale reversible construction, Granular Matter 18 (04 2016). doi:10.1007/s10035-016-0628-y.

[10] A. Dyskin, Y. Estrin, A. Kanel-Belov, E. Pasternak, A new concept in design of materials and structures: assemblies of interlocked tetrahedron-shaped elements, Scripta Materialia 44 (12) (2001) 2689–2694. doi:https://doi.org/10.1016/S1359-6462(01)00968-X.

[11] Y. Estrin, V. R. Krishnamurthy, E. Akleman, Design of architectured materials based on topological and geometrical interlocking, Journal of Materials Research and Technology 15 (2021) 1165–1178. doi:https://doi.org/10.1016/j.jmrt.2021.08.064.

[12] F. Barthelat, Architectured materials in engineering and biology: fabrication, structure, mechanics and performance, International Materials Reviews 60 (8) (2015) 413–430. doi:10.1179/1743280415Y.0000000008.

[13] S. Khandelwal, T. Siegmund, R. J. Cipra, J. S. Bolton, Adaptive mechanical properties of topologically interlocking material systems, Smart Materials and Structures 24 (4) (2015) 045037. doi:10.1088/0964-1726/24/4/045037.

[14] A. Molotnikov, R. Gerbrand, O. Bouaziz, Y. Estrin, Sandwich panels with a core segmented into topologically interlocked elements, Advanced Engineering Materials 15 (8) (2013) 728–731.

[15] Y. Estrin, Y. Beygelzimer, R. Kulagin, P. Gumbsch, P. Fratzl, Y. Zhu, H. Hahn, Architecturing materials at mesoscale: some current trends, Materials Research Letters 9 (10) (2021) 399–421. doi:10.1080/21663831.2021.1961908.

[16] T. Siegmund, F. Barthelat, R. Cipra, E. Habtour, J. Riddick, Manufacture and Mechanics of Topologically Interlocked Material Assemblies, Applied Mechanics Reviews 68 (4) (2016) 040803. doi:10.1115/1.4033967.

[17] A. Molotnikov, R. Gerbrand, Y. Qi, G. P. Simon, Y. Estrin, Design of responsive materials using topologically interlocked elements,

Smart Materials and Structures 24 (2) (2015) 025034. doi:10.1088/0964-1726/24/2/025034.
URL `https://dx.doi.org/10.1088/0964-1726/24/2/025034`

[18] L. Wang, Y. Yang, Y. Chen, C. Majidi, F. Iida, E. Askounis, Q. Pei, Controllable and reversible tuning of material rigidity for robot applications, Materials Today 21 (5) (2018) 563–576. doi:https://doi.org/10.1016/j.mattod.2017.10.010.

[19] A. V. Dyskin, Y. Estrin, A. J. Kanel-Belov, E. Pasternak, Topological interlocking of platonic solids: A way to new materials and structures, Philosophical Magazine Letters 83 (3) (2003) 197–203. doi:10.1080/0950083031000065226.

[20] M. Weizmann, O. Amir, Y. J. Grobman, Topological interlocking in buildings: A case for the design and construction of floors, Automation in Construction 72 (2016) 18–25, computational and generative design for digital fabrication: Computer-Aided Architectural Design Research in Asia (CAADRIA). doi:https://doi.org/10.1016/j.autcon.2016.05.014.

[21] R. Kawamoto, E. Andò, G. Viggiani, J. E. Andrade, Level set discrete element method for three-dimensional computations with triaxial case study, Journal of the Mechanics and Physics of Solids 91 (2016) 1 – 13. doi:https://doi.org/10.1016/j.jmps.2016.02.021.

[22] R. B. de Macedo, E. Andò, S. Joy, G. Viggiani, R. K. Pal, J. Parker, J. E. Andrade, Unearthing real-time 3d ant tunneling mechanics, Proceedings of the National Academy of Sciences 118 (36) (2021). doi:10.1073/pnas.2102267118.

[23] J. M. Harmon, V. Gabuchian, A. J. Rosakis, J. P. Conte, J. I. Restrepo, A. Rodriguez, A. Nema, A. R. Pedretti, J. E. Andrade, Predicting the seismic behavior of multiblock tower structures using the level set discrete element method, Earthquake Engineering & Structural Dynamics 52 (9) (2023) 2577–2596. doi:https://doi.org/10.1002/eqe.3883.

[24] Z. Zhou, M. Andreini, L. Sironi, P. Lestuzzi, E. Andò, F. Dubois, D. Bolognini, F. Dacarro, J. E. Andrade, Discrete structural systems modeling: Benchmarking of LS-DEM and LMGC90 with seismic experiments, Journal of Engineering Mechanics 149 (12) (2023) 04023097.

[25] S. Feldfogel, K. Karapiperis, J. Andrade, D. S. Kammer, Failure of topologically interlocked structures — a level-set-dem approach, European Journal of Mechanics - A/Solids 103 (2024) 105156. doi:https://doi.org/10.1016/j.euromechsol.2023.105156.

[26] S. Feldfogel, K. Karapiperis, J. Andrade, D. S. Kammer, Scaling, saturation, and upper bounds in the failure of topologically interlocked structures, International Journal of Solids and Structures 269 (2023) 112228. doi:https://doi.org/10.1016/j.ijsolstr.2023.112228.

[27] S. Ullmann, D. S. Kammer, S. Feldfogel, The Deflection Limit of Slab-Like Topologically Interlocked Structures, Journal of Applied Mechanics 91 (2) (2023) 021004.

[28] A. S. Dalaq, F. Barthelat, Manipulating the geometry of architectured beams for maximum toughness and strength, Materials Design 194 (2020) 108889.

[29] Y. Tsuji, T. Kawaguchi, T. Tanaka, Discrete particle simulation of two-dimensional fluidized bed, Powder Technology 77 (1) (1993) 79–87. doi:https://doi.org/10.1016/0032-5910(93)85010-7.

[30] X. Tu, J. E. Andrade, Criteria for static equilibrium in particulate mechanics computations, International Journal for Numerical Methods in Engineering 75 (13) (2008) 1581–1606. doi:https://doi.org/10.1002/nme.2322.